Design and Control of a Bio-Inspired Human-Friendly Robot

Dongjun Shin[*], Irene Sardellitti[†], Yong-Lae Park[‡], Oussama Khatib[*], and Mark Cutkosky[‡]

Abstract

The increasing demand for physical interaction between humans and robots has led to the development of robots that guarantee safe behavior when human contact occurs. However, attaining established levels of performance while ensuring safety poses formidable challenges in mechanical design, actuation, sensing and control. To achieve safety without compromising performance, the human-friendly robotic arm has been developed using the concept of hybrid actuation. The new design employs inherently-safe pneumatic artificial muscles augmented with small electrical actuators, human-bone-inspired robotic links, and newly designed distributed compact pressure regulators with proportional valves. The experimental results show that significant performance improvement can be achieved with hybrid actuation over a system with pneumatic muscles alone. The paper simulates and evaluates the safety of the new robot arm and demonstrates that the safety characteristics surpass those of previous human-friendly robots.

1 Introduction

There is a growing interest in human-friendly robotics involving close physical interaction between robots and humans. With the ability to support a variety of commercial uses, applications for human friendly robots have emerged in medicine, home care, manufacturing and entertainment. A major challenge in such applications is safety: How can robots be sufficiently fast, strong, and accurate to do useful work while also being inherently safe for physical interaction?

Robots have traditionally relied on electromagnetic actuators, which offer excellent controllability but poor power-to-weight ratios compared to pneumatic muscles [3, 6, 25]. Even more limiting is their inability to exert large sustained forces without high transmission ratios between the motor and the load. The high transmission ratios result in robot arms with high mechanical impedance, which are inherently less safe than their biological counterparts when unexpected contacts occur. Previous efforts to increase the safety of robot arms while maintaining control performance
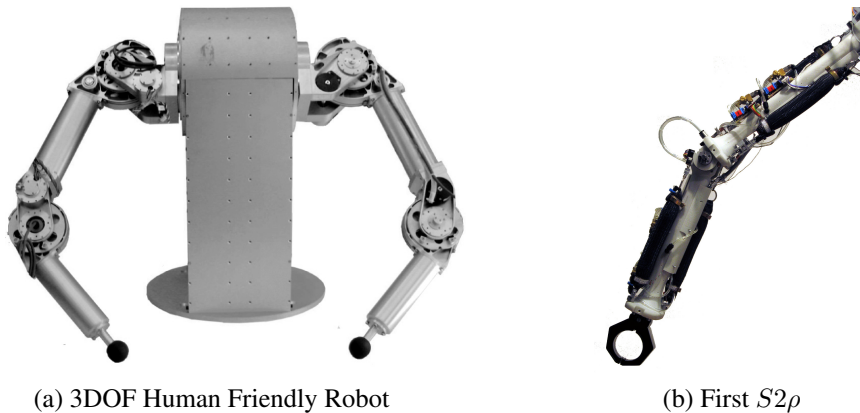

(a) 3DOF Human Friendly Robot   (b) First $S2\rho$

Figure 1: (a) Distributed Macro-Mini Actuation, DM^2, approach achieves a significant increase in the control bandwidth and reduction in the effective inertia [36]. (b) Stanford Safety Robot, $S2\rho$, provides light yet powerful actuation and reduces complexity of design and manufacturing[22].

[*]Artificial Intelligence Laboratory, Stanford University, Stanford, CA 94305, USA. {djshin, ok}@robotics.stanford.edu

[†]Advanced Robotics Laboratory, Italian Institute of Technology, Genoa, Italy. irene.sardellitti@iit.it

[‡]Department of Mechanical Engineering, Stanford University, Stanford, CA 94305, USA. {ylpark, cutkosky}@stanford.edu

1

have included relocating the actuators to the base and powering the joints with cables[19], designing links with high-strength composite and employing a series elastic actuator [18]. Other work have employed variable compliance [2, 8, 13, 21, 28] and/or compliant, energy-absorbing layers and proximity sensors to detect impending collisions [16]. Approaches based on artificial pneumatic muscle alone have also been proposed [27, 31]. Other strategies which adopt two actuators for each degree-of-freedom have included employing parallel-coupled macro and micro actuators [14], and controlling the stiffness and joint position with an individual actuator for each respective property [29, 33]. A summary of current challenges and technologies for human-safe robotics is provided in [1]. In addition, the effective evaluation of robot safety has been discussed in [9, 10].

1.1 Hybrid Actuation for Human Friendly Robot

Our efforts in developing the human-friendly robot over the past several years at the Stanford AI Lab produced Distributed Macro-Mini (DM^2) actuation, which provides a combination of high power, low impedance, and precise control as shown in the Fig. 1 (a) [34, 35]. Large (macro), low frequency actuators are located at the base of the robot arm as the main source of mechanical power; mini actuators are located at the joints for fast response. The 3DOF platform with the DM^2 actuation achieves a significant increase in the control bandwidth and reduction in the effective inertia [24]. However, the poor power density of electrical actuators still requires high gear ratios, which result in a heavy and bulky system not suitable for a mobile platform. Furthermore, cable transmissions increase the complexity of design and assembly.

Recent studies on powerful yet light actuation have developed hybrid actuation, which further reduces design and assembly complexity. The Stanford Safety Robot, $S2\rho$, employs the hybrid actuation combining powerful pneumatic actuators with small electrical actuators in a parallel configuration at each joint as shown in Fig. 1 (b) [22]. Key features embodied in the $S2\rho$ include: replacement of heavy electrical actuators with compliant pneumatic muscles; utilization of compact pressure regulators within the links; and integration of valves, actuators and electronics around a sculpted, bone-like structural element. The pneumatic muscle enables the prototype arm to be light, compact, and
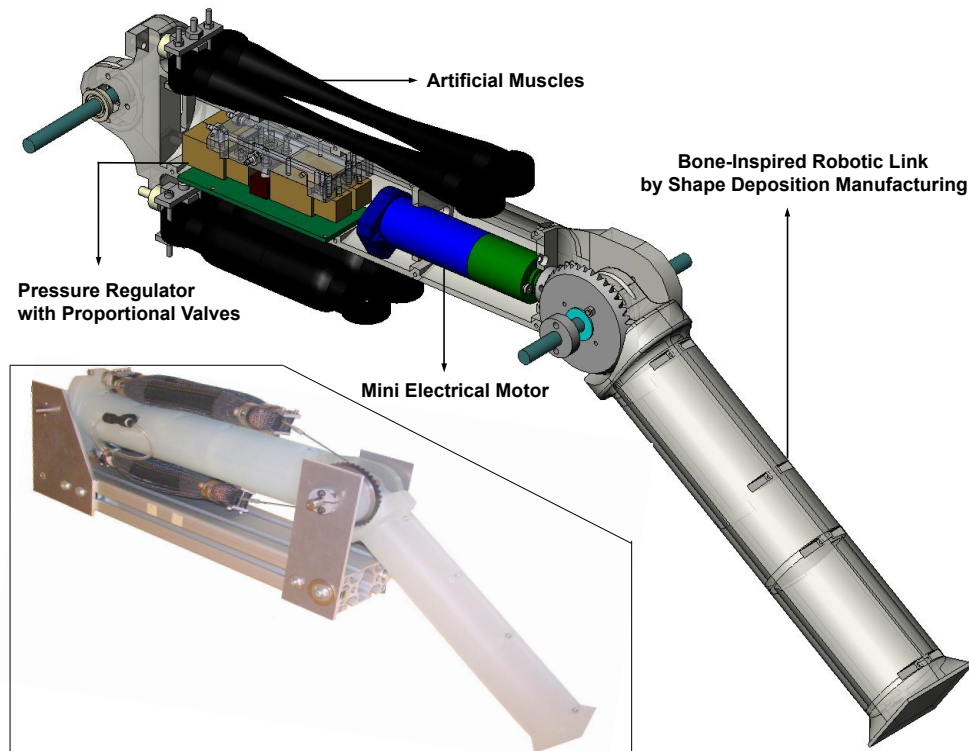

Figure 2: New Stanford Safety Robot (a new 1-DOF prototype)

compliant due to its high force-to-weight ratio and air compressibility. The distributed compact pressure regulators decrease air flow resistance and line capacitance, and reduce the complexity of the arm by being located adjacent to the actuators. The human-bone-inspired robotic link further reduces the inertia and simplifies design and manufacturing process. As a result of continuous efforts in improving the first $S2\rho$ robotic arm, we have developed $S2\rho_{ver1.5}$[23]. The new design incorporates multiple parallel pneumatic actuators at each joint to increase the range of motion and available torque without becoming bulky. The actuators are controlled by a new proportional valve system for fast response and smooth force control. The valves, along with the mini actuators and other components, are housed in a new thin-walled structure that provides a combination of light weight and robustness. The results of our continuing experimentation and redesign on the new $S2\rho$ are shown in Fig. 2.

This paper presents the details of the actuation and the robotic structure of the new $S2\rho$ in Section 2. The control strategy and design process are described in Section 3, followed by experimental and analytical results in Section 4. Finally, the paper provides a conclusion and discussion of future work in Section 5.

2 Design

2.1 Actuation

The first-generation $S2\rho$ robotic arm uses a single pair of McKibben artificial muscles as macro actuators, taking advantage of their high power-to-weight ratio and intrinsic compliance. Pairs of muscles are used in an antagonistic configuration, pulling on a cable that wraps around a pulley at the joint. A limitation of McKibben muscles is that they have a modest ($\approx 22\%$) contraction ratio. At the shoulder and elbow, respectively, they are used with 61.0 mm and 40.6 mm diameter pulleys, resulting in 58 and 86 degrees of rotation to produce a desired 6.10 Nm and 4.06 Nm of torque. To overcome this limitation, the new design (Fig. 2) uses multiple McKibben muscles in parallel on each side of the pulley to provide a higher force without excessive bulk and time to fill and exhaust the muscle chambers. Using a 40.6 mm pulley for a maximum torque of 8.12 Nm, the new configuration achieves 127 degrees of rotation with appropriate pre-tension.

To meet size and weight requirements, the former robotic arm employs 4.5g small on-off solenoid valves (X-Valve, Parker) to actuate the muscles, with one valve for pressurizing and three for exhausting, to compensate for the lower air pressure drop and air flow rate of the exhaust [30]. However, these compact valves result in a performance limitation in a transient and steady state operation. The restricted flow rate (effective orifice size: 0.51 mm) causes substantial errors in transient response. In addition, their on-off behavior produces undesirable overworking and/or oscillation in steady state operation, especially at high pressure. The new design exploits valves (MD Pro, Parker) with higher flow rates (effective orifice size: 1.27 mm) and a proportional flow control feature. To match the flow rates between pressurizing and exhausting, higher flow rate valves (effective orifice size: 1.79 mm) are employed for exhausting. As shown in Fig. 3 (a) and (b), the proportional valves achieve a significantly faster initial response and a faster convergence to the desired pressure. (Note that the pressurizing and exhausting phases present an asymmetrical behavior resulting from

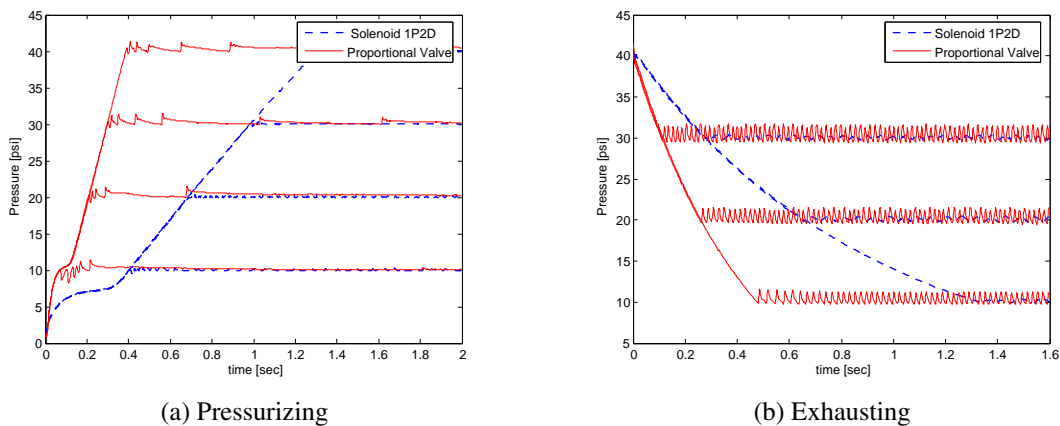
(a) Pressurizing   (b) Exhausting

Figure 3: Step response comparison between proportional valve and the array of solenoid valves for pressurizing (a) and exhausting (b) phases. The array of solenoid valves has one pressurizing valve and two exhausting valves to compensate asymmetrical behavior due to different pressure drop across the valves [22].

3

(a) Step Response at Pressurizing (b) Step Response at Exhausting (c) Steady State Error comparison
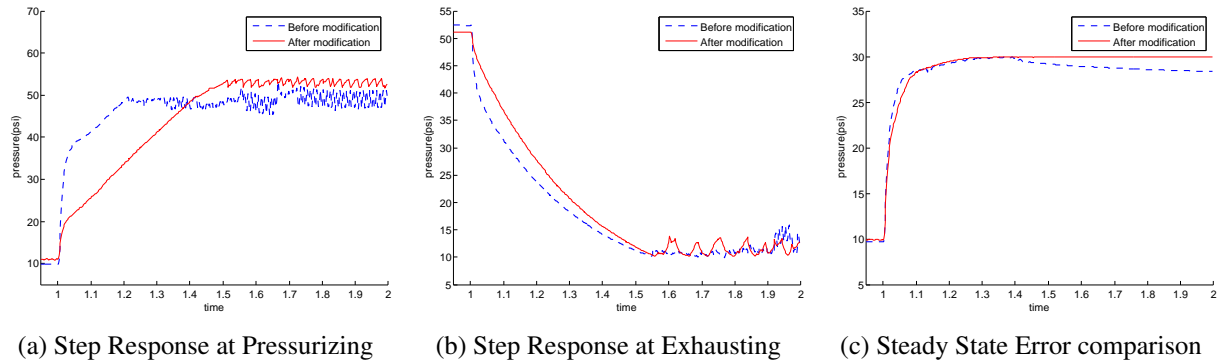
Figure 4: Pressure step responses for filling (a) and exhausting (b) show the effect of modifying the manifold so that the measured pressure more accurately reflects muscle pressure, which rises more slowly than pressure at the valve. Before manifold modification, the measured pressure is almost constant instead gradually equalizing between the muscles and manifold-attached sensor when both pressurizing and exhausting valves are closed (c).

the different pressure drops across the valves.) The faster response achieved with proportional valves results in the significantly improved joint torque control as discussed in Section 4.

To accommodate the valves, pressure sensors and driving circuit, a new customized manifold was designed and fabricated using Shape Deposition Manufacturing (SDM) [32], a rapid prototyping process that has been used for bio-inspired robots [5]. As a result of some separation between the interior of the muscle and the valve, there is an inevitable pneumatic delay, which affects response. The effects of back pressure are minimized by increasing the diameter of air tube and reducing the length of air path in the manifold. Figures 4 (a) and (b) show that the initial rapid change, which results from the effects of back pressure, is greatly reduced during pressurizing and exhausting. Figure 4 (c) demonstrates that the manifold modification achieves a smaller measured drop in a steady state operation, where both pressurizing and exhausting valves are closed while the pressure is controlled in Fig. 4 (a) and (b). (Before the manifold modification, the measured pressure between the muscles and the manifold-attached sensor gradually equalizes when all valves are closed.) As a result of these modifications, measurement errors are reduced and the sensor pressure reflects the muscle pressure more accurately.
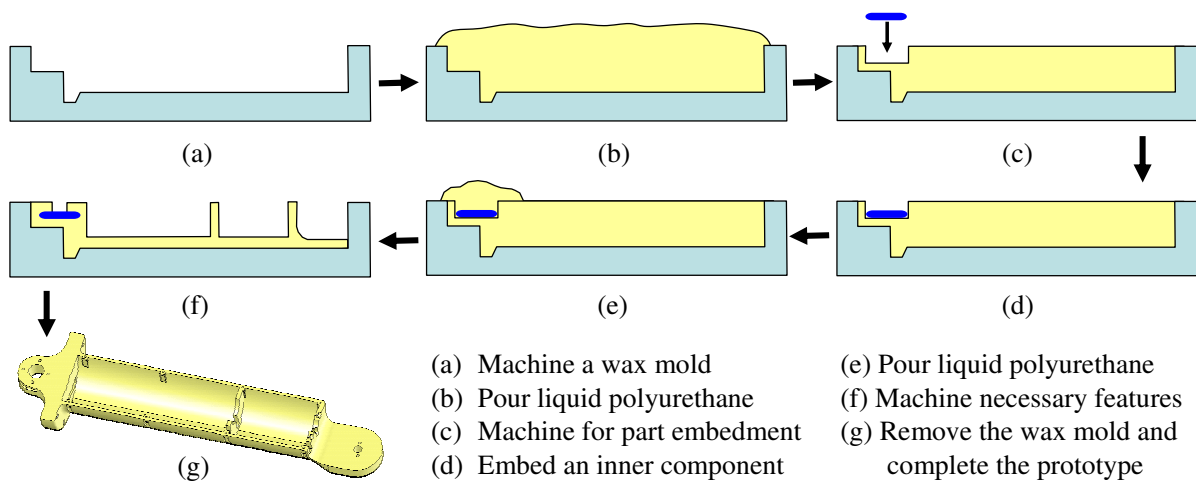

(a) Machine a wax mold   (e) Pour liquid polyurethane
(b) Pour liquid polyurethane (f) Machine necessary features
(c) Machine for part embedment (g) Remove the wax mold and
(d) Embed an inner component   complete the prototype

Figure 5: SDM process to build half structure of upper arm

2.2 Materials and structures

The first-generation $S2\rho$ robotic arm used a polymer structure as the central bone-like support. The structure was created using selective laser sintering (SLS) with glass-filled nylon. While SLS allows almost arbitrary shapes to be realized, the resulting parts are not particularly strong for their weight. The new arm is created using SDM, which allows combinations of hard and soft materials, as well as sensors and other discrete parts, to be integrated in a single heterogeneous structure. The new link is a thin-walled shell (Task 9, Shore 85D polyurethane) that houses the valves, mini actuator, controllers and wiring. The tolerances with SDM are sufficient for aligning the motor and gears at the joint. The SDM fabrication process to build a half structure of an upper arm is shown in Fig. 5, and a complete prototype with this procedure is shown in Fig. 6. Inner components can be embedded during intermediate machining and pouring steps. To create a conduit for the cable that is pulled by the Mckibben actuators, a hollow nylon tube was embedded in the pulley, and part of it was removed as shown in Fig. 7.

3 Control Strategy

The $S2\rho$ robotic arm is controlled employing a pair of actuators, connected in parallel. The controller partitions the reference input torque between low frequency actuation (macro actuation) and high frequency actuation (mini actuation) based on the frequency. For the low frequency actuation, low impedance output is achieved by using the light pneumatic muscles. For the high frequency actuation, low impedance is achieved by using a small low-inertia motor connected to the manipulator through low-ratio gear transmission. This combination reduces the inertia of the arm and increases the bandwidth for closed-loop control. However, the first-generation $S2\rho$ robotic arm showed limited performance resulting from the slow dynamics of the macro actuation, which could not be overcome entirely by the electric actuator. The electric actuator tended to saturate, resulting in a temporary degradation of performance and stability. Furthermore, the limited stroke of the pneumatic muscles decreased the range of motion. To address these problems, the new prototype employs new macro actuation with multiple muscles in parallel and proportional valves, which provide a better tradeoff among power-to-weight ratio, response time, and control accuracy.
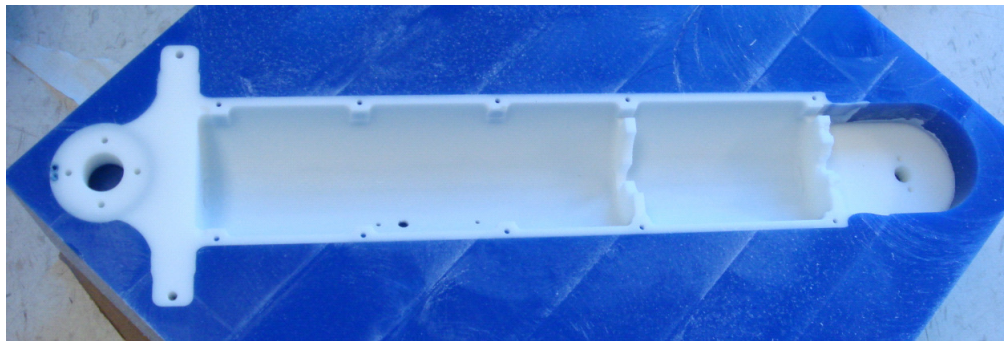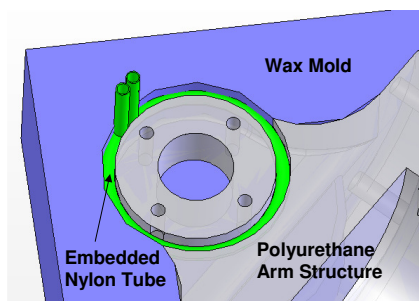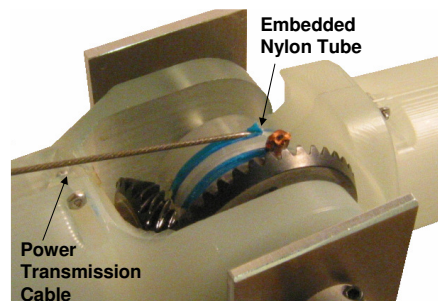

Figure 6: Complete half structure of upper arm before removing wax mold

(a) SDM process for embedding nylon tube

(b) Embedded nylon tube for cable

Figure 7: To create a conduit for the cable that is pulled by the Mckibben actuators, a hollow nylon tube was embedded in the pulley, and part of it was removed.
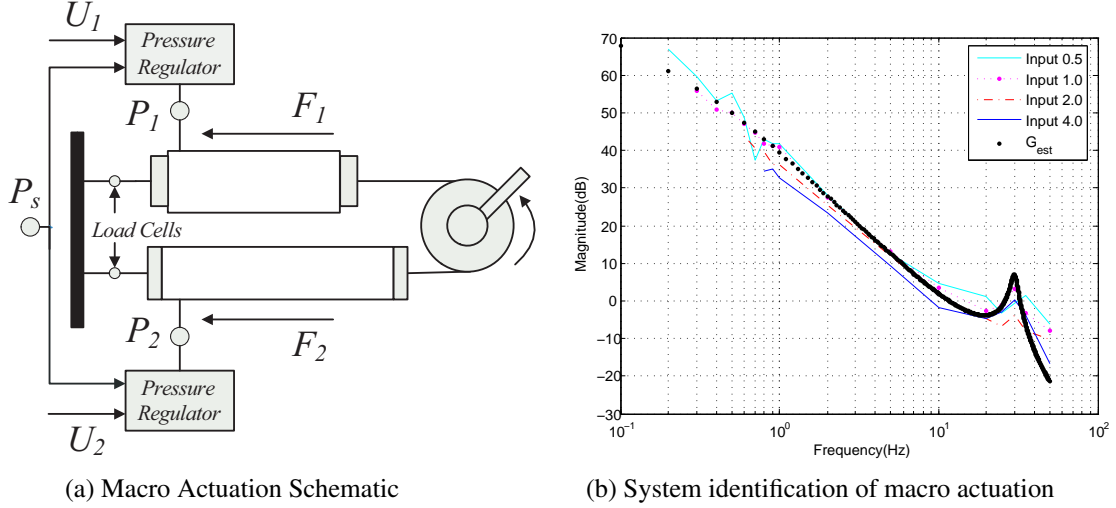
(a) Macro Actuation Schematic   (b) System identification of macro actuation

Figure 8: (a) The macro actuation system includes the pressure regulator and muscles. $P_1(P_2)$, $U_1(U_2)$, $F_1(F_2)$ and P_s denote regulated muscle pressures, muscle forces, command signal and supply pressure, respectively. (b) Bode plot of the estimated macro actuation system. The results indicate that equations (3) and (4) are good approximations for the system input voltage between 0.5 V and 3 V. For an input of 4 V, the system deviates from the predicted Bode plot due to saturation of the pressure regulator.

3.1 Macro Actuation

The macro actuator is an antagonistic pair of pneumatic muscles as shown in Fig. 8 (a) [20]. When a desired torque is to be produced for the joint, the necessary force difference is symmetrically distributed between the two antagonistic muscles and controlled by force feedback through load cell measurements as shown in Fig. 11 (a). The force feedback compensates for the pneumatic muscle force/displacement hysteresis phenomenon while also increasing the actuation bandwidth [20].

In order to design the controller, system identification was first conducted to identify the dynamic behavior of the pneumatic muscles and proportional valves. The proportional valve operates based on the balance between the magnetic force and mechanical force on the spool; when the magnetic force overcomes the pressure, the valve opens. However, since the mechanical force increases as pressure across the valve rises, an experiment was conducted to identify the threshold voltage to open the valve as a function of the muscle pressure. With respect to the pressure of the muscle, P, the threshold voltages, V_{th}, for pressurizing valves and exhausting valves can be approximated with the linear equations as

$$V_{th} = -0.013 \times P + 2.376 \quad : \text{Pressurizing Valve} \tag{1}$$

$$V_{th} = 0.031 \times P + 1.320 \quad : \text{Exhausting Valve} \tag{2}$$

Since the mechanical force of the valve is provided by a spring-damper system, the dynamics between the input voltage, U, and flow rate, Q, can be approximated for low frequencies using an integrator with a second order dynamics [12]. The pneumatic muscles can be approximated by a first order system experimentally [20]. Thus, the transfer function of the entire macro actuation system, G_{macro}, which is the merged system of valves and muscles, is given by

$$
\begin{aligned}
G_{macro} \quad = G_{valve} \cdot G_{muscle} \quad &= \frac{X}{U} \frac{Q}{X} \cdot \frac{P}{Q} \frac{F}{P} \\
&= K_{valve} \frac{s + z_{valve}}{s(s^2 + 2\zeta\omega + \omega^2)} \cdot K_{muscle} \frac{s + z_{muscle}}{\tau s + 1}
\end{aligned} \tag{3}
$$

where, X, P, F, K_{valve}, and K_{muscle} are valve spool position, muscle pressure, muscle force, system gain of the valve, and system gain of the muscle, respectively. z_{valve} and z_{muscle} are zero of valve and muscle, respectively, which are obtained experimentally.

To identify the macro actuation system as shown in Fig. 8 (a), sinusoidal inputs with various frequencies were used. Although the system includes manifold and tube dynamics, which are hard to measure, the experimental results
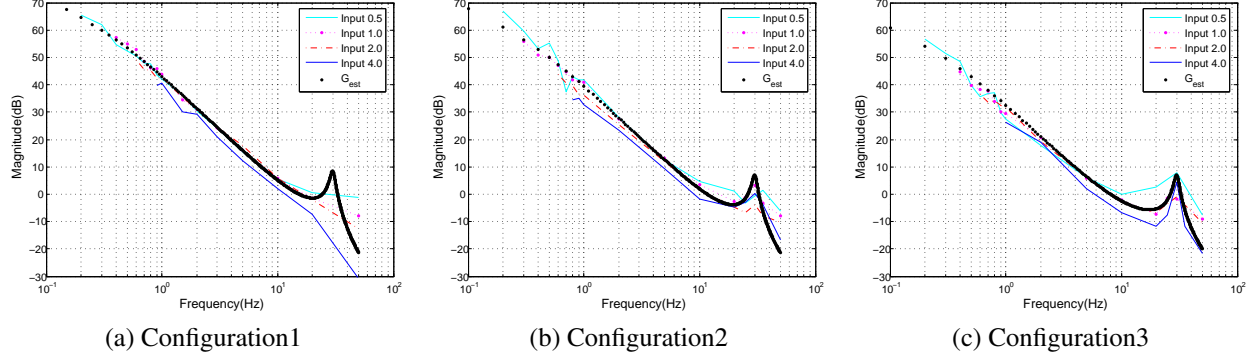
6

(a) Configuration1   (b) Configuration2   (c) Configuration3

Figure 9: System identification with various joint configurations. The order of macro actuation system, G_{macro}, is maintained as the system gain changes. The gain with respect to the joint configuration is fit with a cubic spline. $q = -18.34^o$, 1.94^o, and 29.80^o for configuration 1, 2 and 3, respectively.

indicate that equations (3) is good approximation for the system input voltage between 0.5 V and 3 V. However, as seen in Fig. 8 (b), for an input of 4 V, the curve deviates from the prediction due to saturation of the pressure regulator. The lumped parameter values at joint angle, q, of 1.94^o are:

$K = K_{valve} \cdot K_{muscle}$	100	τ	2.5
ζ	0.1	ω	28
z_{muscle}	20	z_{valve}	30

Experiments with respect to different configurations, which are associated with joint angles, demonstrate that muscle dynamics depend on muscle length. Fig. 9 shows the system order is maintained while the system gain changes. ($q = -18.34^o$, 1.94^o, and 29.80^o for configuration 1, 2 and 3, respectively). The system gain with respect to the joint angle is fit with a cubic spline:

$$K = -4.2 \times 10^{-4}q^3 + 7.4 \times 10^{-3}q^2 + 1.5q + 97 \tag{4}$$

A non-linear effect is observed for low amplitude input commands. Fig. 10 (a) and (c) shows that the actual system is well matched by the estimated system, even at high frequency, when pneumatic muscle initially contains air at low pressure. However, at higher initial pressure, the actual system is less well approximated by the estimated system, especially with small inputs at high frequency as shown in Fig. 10(b) and (d). These results are expected, as the pressure regulator flow rate is governed by the equation,

$$Q = CX\sqrt{\Delta P} \tag{5}$$

where Q, C, X, and ΔP are the flow rate of pressure regulator, the flow constant, the plunger/spool position, and the pressure difference across the regulator, respectively [12]. At higher pressures, the pressure difference seems to dominate the flow rate rather than the small plunger/spool displacement corresponding to small input command. Furthermore, the response of the plunger/spool is limited at high frequency. In the next section, we discuss how we accommodate this nonlinear effect in the hybrid control strategy.

Among the tested compensators, based on the previously described system identification, a PID controller provides the best performance. A PI controller has good tracking performance, but significant phase delay at high frequency and a PD controller has significant tracking errors. Fig. 11 (a) demonstrates that the compensator gain of the macro force control is adapted with respect to the configuration, which is associated with the lengths of the pneumatic muscles. The PID controller with adaptive gain in frequency domain is given by

$$C = \frac{22.5}{K} \frac{s+6}{s+300} \frac{s+25}{s+0.01} \tag{6}$$

where, K is given by equation (4).

(a) Configuration2 at 16psi

(b) Configuration2 at 40psi

(c) Configuration3 at 16psi
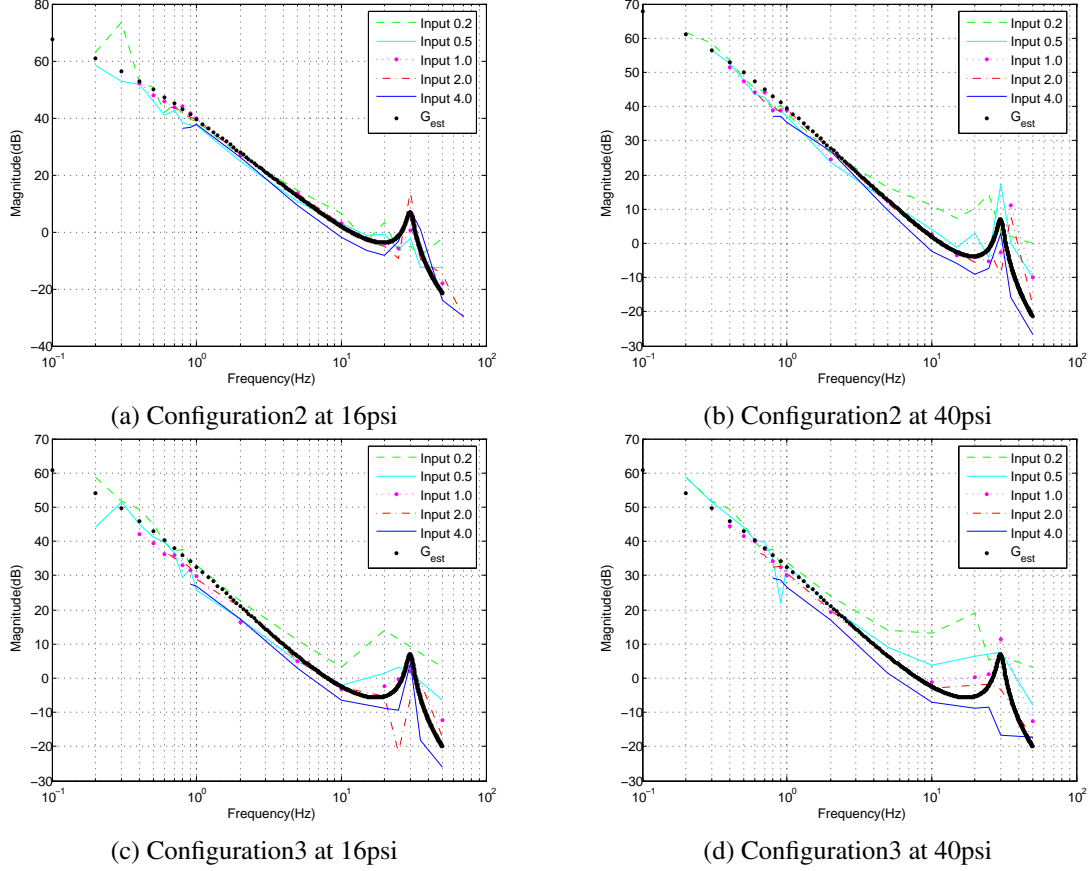

(d) Configuration3 at 40psi

Figure 10: System identification with various initial pressures. Fig. (a) and (c) shows the actual system is well matched by the estimated system when the pneumatic muscle initially contains air at low pressure. However, at higher initial pressure, the actual system differs from the estimated system, especially with a small input at high frequency as shown in Fig. (b) and (d).

Chou developed the analytical model of the pneumatic muscle as

$$F = \frac{Pb^2}{4\pi n}(\frac{3L^2}{b^2} - 1) \tag{7}$$

where, F, P, and L are force, pressure, and length of the muscle, respectively. The terms, b and n, are muscle constants [6]. Although this model has been widely used in a number of robotic arms utilizing pneumatic muscles, the model predicts a different force output from what was measured since the model does not account non-linearities of pneumatic muscles. Previous efforts to develop an adequate yet simple model include introducing an effectiveness term [7], and modeling precise friction model [25, 26]. However, the viscous friction and air compressibility produce high non-linearity, which substantially depends on the length of muscles. Furthermore, the difficult measurement of muscle constants raises another possibility of error. These problems consequently result in inconsistent open-loop control performance at different configurations, which are associated with the muscle lengths. The closed loop PID control with force feedback through a load cell significantly compensates high non-linearity and inconsistency while improving force control performance over the open-loop control that uses the pneumatic muscle analytical model alone [20]. As shown in Fig. 12, the closed loop PID control works successfully at 6Hz, the bandwidth of the macro closed loop force control, while the open-loop control shows significant deviation from a reference input command.

3.2 Hybrid Actuation

The hybrid actuation control scheme adopts dual actuation with macro and mini actuation. The hybrid actuation controller separates commanded torques into the macro, i.e., pneumatic muscles, and the mini, i.e., electrical motor, on the basis of frequency content. The torque applied on the joint will then be the linear combination of the macro

8
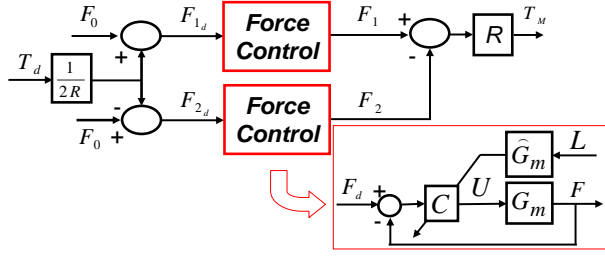
(a) Macro torque control with adaptive force control
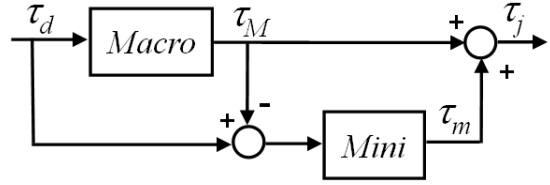
(b) Hybrid Actuation

Figure 11: (a) The block, Force Control, represents an individual muscle adaptive force controller. This demonstrates that the compensator gain of macro force control is adapted with respect to the configuration, i.e., the pneumatic muscles length. R and L denote the radius of the pulley and the length of muscle, respectively. (b) The torque applied on the joint will then be the linear combination of the macro and mini torque contributions. Mechanical advantages such as low gear reduction ratio and near-collocated actuator allow us to assume that desired torque is achieved at the joint. The faster dynamics of the mini actuator compensate for the slow dynamics of the pneumatic muscle.

and mini torque contributions, as shown in Fig. 11 (b). For the mini controller, an open-loop torque controller is implemented. The measured torque error of the macro actuation is directly commanded to the mini actuation. Mechanical advantages such as low gear reduction ratio and near-collocated actuator allow us to assume that the desired torque of the mini actuation is achieved at the joint. The faster dynamics of the mini actuation compensate for the slow dynamics of the macro actuation.

4   Experimental Results

In order to validate the hybrid actuation concept for the human friendly robot, we built a one-degree-of-freedom testbed as explained in Sec. 2 and shown in Fig. 2. For performance analysis, open-loop contact force tests with hybrid actuation and position control with hybrid actuation were conducted. For safety analysis, the normalized effective mass was simulated and compared to other robotic arms.
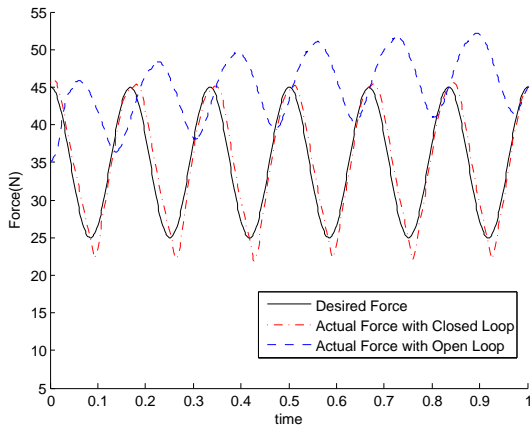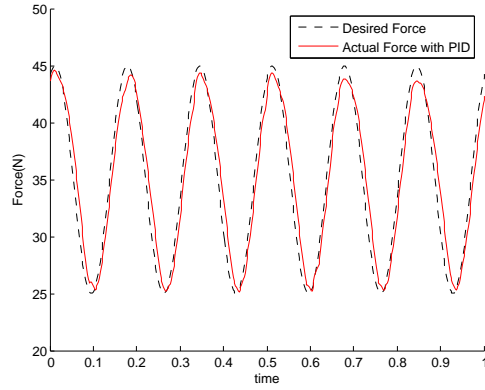

(a) Macro Force Control at Configuration 2
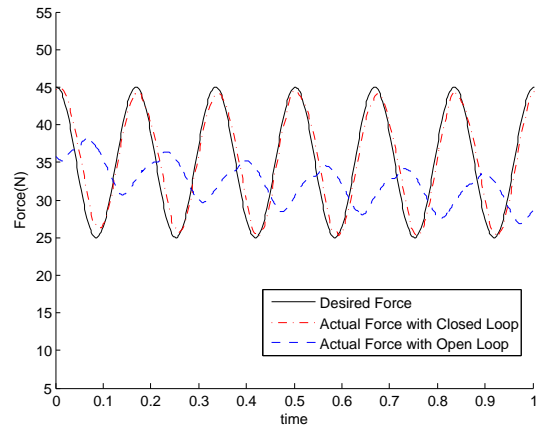
(b) Macro Force Control at Configuration 3

Figure 12: Macro force control comparison for open-loop and closed loop control at 6Hz, the bandwidth of the macro closed loop force control. Closed-loop PID control with force feedback through a load cell significantly improves force control performance over the open-loop control that uses the pneumatic muscle analytical model alone [20]. Fig. (a) and (b) demonstrate the force feedback PID control tracks the reference input consistently regardless of the muscle length, while the open-loop control shows significant deviation from reference input command and different behavior depending on the muscle length.
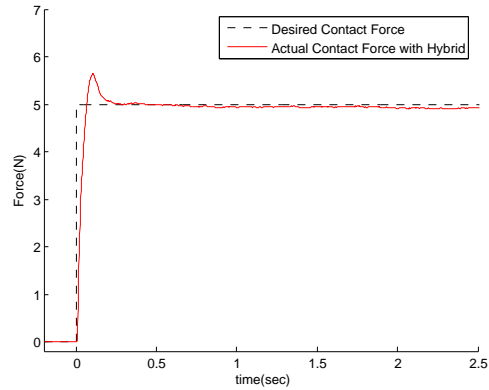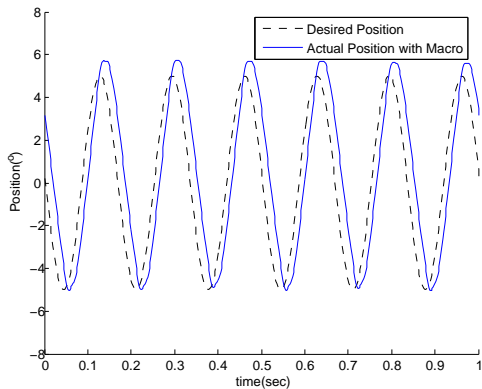
9
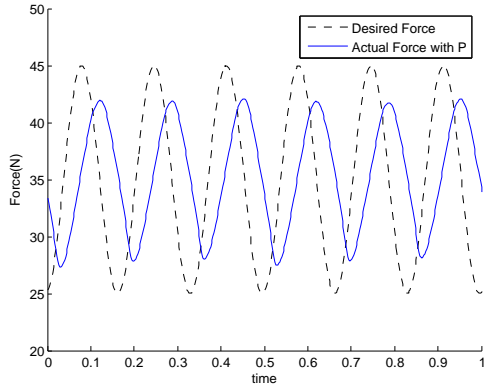
(a) Macro Force Control with a P controller

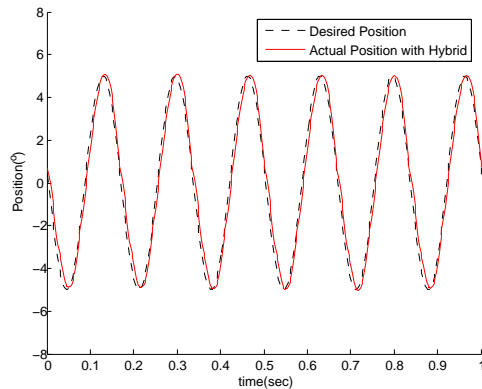(b) Macro Force Control with a PID controller
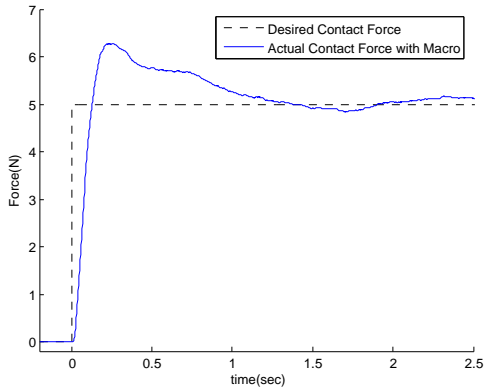
(c) Contact Force Control with macro actuation

(d) Contact Force Control with hybrid actuation

(e) Position Control with macro actuation

(f) Position Control with hybrid actuation

Figure 13: (a) and (b): Force control comparison for P and PID controller at 6Hz. PID shows better performance at higher frequency in tracking error and phase delay. (c) and (d): Open-loop contact force control comparison for macro and hybrid control. Hybrid actuation achieves a bandwidth of 26Hz while macro actuation achieves 6Hz. A negligible steady state error of contact force with hybrid actuation demonstrates that mini actuation works successfully without closed loop control. (e) and (f): Position tacking control comparison for macro and hybrid control with a sinusoidal reference input (10 degrees at 6Hz). Hybrid actuation shows significant improvement over the system with macro actuation alone. The results also demonstrate that the new design and control overcome the performance limitations of the first-generation $S2\rho$.

4.1 Performance Characteristics

In order to verify the performance of macro actuation, experiments were conducted comparing a simple P controller and the PID controller. As shown in the Fig. 13 (a) and (b), PID shows better performance at high frequency in terms of tracking error and phase delay.

Since load cell measures not final joint torque but pneumatic muscle force, the mini actuator does not affect load cell measurement at a fixed configuration. Therefore, the contact force at the end-effector is measured with an external force sensor to verify the effect of the mini actuator in force control at a given configuration. Figures 13 (c) and (d) show the performance difference between the macro actuation alone and hybrid actuation. Hybrid actuation achieves a force control bandwidth of 26Hz while macro actuation achieves 6Hz. A negligible steady state error of contact force with hybrid actuation demonstrates that open-loop torque control is satisfactory for the mini actuator.

In addition, experiments of position tracking at increasing frequency were conducted. A position controller was implemented as an outer loop wrapped around the inner hybrid actuation controller. The desired torque of the hybrid actuation controller is given by

$$\tau_d = A(\ddot{q}_d - k_p(q - q_d) - k_v(\dot{q} - \dot{q}_d)) \tag{8}$$

where, $\ddot{q}_d$ is the desired acceleration, q_d and q are the desired and actual joint position, $\dot{q}_d$ and $\dot{q}$ are the desired and actual joint velocity, and A is the inertia matrix. Position tracking experiments were conducted for the macro actuation and the hybrid actuation. In Figures 13 (e) and (f), the position tracking control of the macro and the hybrid actuation are plotted for a sinusoidal reference input, of which frequency is 6Hz and amplitude is 10°. The result shows that the hybrid actuation control shows significant performance improvement over the macro actuation alone in compensating for the non-linear effect of the pneumatic muscles. In addition, the results demonstrate that the new design and control scheme of $S2\rho$ overcomes the performance limitations of the first-generation $S2\rho$, for which the position control bandwidth was 2Hz [22].

4.2 Safety Characteristics

Since safety is the main requirement of human friendly robot development, it is desirable to establish quantitative criteria for comparing among robots. Robot safety is a function of impact velocity, interface stiffness between the robot and human, and effective inertia [34]. The impact velocity depends on maximum joint velocity, which is intrinsically bounded by actuator dynamic specifications. The compliance and damping of the robot skin are also critically important design parameters, but beyond the scope of this paper. For a given impact velocity and angle, the remaining critical parameter is the effective inertia, which can be graphically illustrated as a belted ellipsoid over the workspace plane [11]. Figures 14(a) and (b) display the effective mass at the same shoulder and elbow configurations for a PUMA560, the DM^2, human and the S2ρ. The diagram demonstrates that the effective hybrid actuation approach reduces the effective mass by approximately a factor of two compared to the previous DM^2. The S2ρ robotic arm has
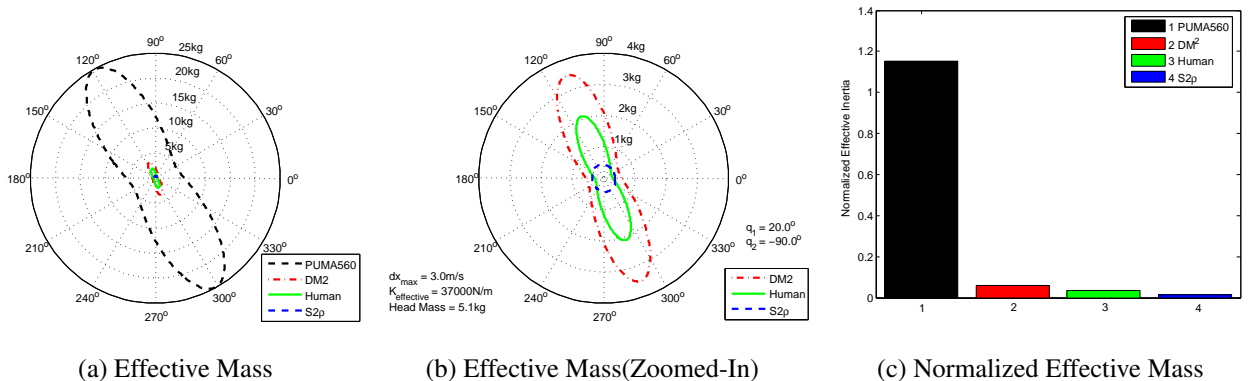

(a) Effective Mass   (b) Effective Mass(Zoomed-In)   (c) Normalized Effective Mass

Figure 14: (a) and (b) Effective mass of PUMA560, DM^2, S2ρ and Human. S2ρ has a maximum effective mass of 0.4kg as compared to 3.5kg for DM^2 and 2.2kg for the Human, while the conventional PUMA560 has an effective mass of 25kg. (c) Normalized effective Inertia. Effective inertia is normalized by payload for better comparison. The PUMA560 has a normalized effective mass of 1.15 but S2ρ shows only 0.015.

a maximum effective mass of 0.4kg as compared to 3.5kg for DM^2, while a conventional robot such as PUMA560 has the far greater effective mass of 25kg.

However, a lower effective mass may come at the expense of reduced performance if the lower effective mass is a consequence of using lower gear ratios and smaller actuators. Therefore, the safety analysis needs to incorporate additional constraints that enable comparisons among manipulators at the same level of performance. As shown in the Fig. 14 (c), the effective mass of each robotic arm is normalized by its own payload, so that the safety comparison between robotic arms with different size/payload can be made. While the PUMA560 and DM^2 have normalized effective masses of 1.154 and 0.058, $S2\rho$ shows only 0.015. The improved result compared to the previous DM^2 approach shows that the safety of $S2\rho$ is not compromised by an additional actuator, i.e., the pneumatic muscle. For an additional comparison, we provide the normalized effective mass of an average U.S. male civilian arm, which is sampled from surveys of U.S. populations [4, 15].

5   Conclusion and Future Work

The concept of hybrid actuation is presented with a revised version of the Stanford Safety Robot Arm, referred as to $S2\rho$. Additional pneumatic muscles connected in parallel provide a wider range of motion without sacrificing the joint torque and response time. New pressure regulators with proportional valves improve the response time in transient conditions and reduce steady state errors. A new manufacturing method, Shape Deposition Manufacturing, enables the integration of power sources as well as mechanical components so that the system can be lighter, stronger and more compact. A PID force feedback control with the load cell improves the performance of macro actuation and confirms the system identification for various muscle conditions. Used in combination with open-loop torque control for the mini actuator, the hybrid system shows significant performance improvement over the arm with pneumatic actuation alone. Safety simulations using the normalized effective mass/inertia validate the arm safety characteristics, which are comparable to those of a human arm.

Future versions of the robot arm structure will include fiber reinforcement for higher specific strength and embedded sensors to measure loads on the arm, following the approach used in [17]. The arm will also be covered with a compliant skin with embedded sensors communicating over a network. In terms of control, the analysis of stiffness characteristics and interference between macro and mini actuation will be conducted.

6   Acknowledgements

References

[1] A. Bicchi, M. Peshkin, and J.E. Colgate. Safety for physical human-robot interaction. *Springer Handbook of Robotics 2008*, pages 1335–1348, 2008.

[2] A. Bicchi and G. Tonietti. Design, realization and control of a passively compliant robot for intrinsic safety. *IARP/IEEE-RAS Joint Workshop on Technical Challenge for Dependable Robots in Human Environment*, 2002.

[3] D. G. Caldwell, G. A. Medrano-Cerda, and M. J. Goodwin. Control of pneumatic muscle actuators. *IEEE Control Systems Magazine*, 15(1)(1):40–48, 1995.

[4] D. Chaffin, G. Andersson, and B. Martin. Occupational biomechanics. *Fourth Edition, Wiley*, 2:47–49, 2006.

[5] J. G. Cham, J. C. Bailey, S. E. andClark, Full R. J., and Cutkosky M. R. Fast and robust: Hexapedal robots via shape deposition manufacturing. *International Journal of Robotics Research*, 21(10-11):869–882, 2002.

[6] Hannaford B. Chou, C.P. Measurement and modeling of mckibben pneumatic artificial muscles. *IEEE Robotics and Automation Magazine*, 12(1):90–102, 1996.

[7] R.W. Colbrunn, G. M. Nelson, and R. D. Quinn. Modeling of braided pneumatic actuators for robotic control. *Proceedings of the 2001 IEEE/RSJ International Conference on Intelligent Robots and Systems*, 4:1964–1970, 2001.

[8] C.E. English and D. Russell. Mechanics and stiffness limitations of variable stiffness actuator for use in prosthetic limbs. *Mechanism and machine theory*, 34(1), 1999.

[9] S. Haddadin, A. Albu Schaffer, and G. Hirzinger. Safety evaluation of physical human-robot interaction via crash testing. *Robotics: Science and Systems Conference*, 2007.

[10] S. Haddadin, A. Albu Schaffer, and G. Hirzinger. The role of the robot mass and velocity in physical human-robot interaction - part i: Unconstrained blunt impacts. *IEEE Int. Conf. on Robotics and Automation, Pasadena, USA, 2008*, pages 1331–1338, 2008.

[11] O. Khatib. Inertial properties in robotic manipulation: An object-level framework. *International Journal of Robotics Research*, 14(1):19–36, 1995.

[12] M. Kontz. Haptic control of hydraulic machinery using proportional valves. *PhD thesis, Georgia Institute of Technology, Atlanta, GA*, 2007.

[13] S.A. Migliore and DeWeerth S.P. Brown E.A. Biologically inspired joint stiffness control. *IEEE International Conference on Robotics and Automation*, pages 4508–4513, 2005.

[14] J. B. Morrel. Parallel coupled micro-macro actuators. *PhD thesis, Massachusetts Institute of Technology, Cambridge, MA*, 1996.

[15] NASA. Man-systems integration standards. *NASA-STD-3000*, 1:Section 4, 1995.

[16] J.L. Novak and I.T. Feddema. A capacitance-based proximity sensor for whole arm obstacleavoidance. *Proc. of the 1992 IEEE International Conference on Robotics and Automation*, 2:1307–1314, 1992.

[17] Y-L. Park, K. Chau, R. J. Black, and M. R. Cutkosky. Force sensing robot fingers using embedded fiber Bragg grating sensors and shape deposition manufacturing. *Proc. of the 2007 IEEE International Conference on Robotics and Automation*, pages 1510–1516, 2007.

[18] G. Pratt and Williamson M. Series elastic actuators. *Proc. of the 1995 IEEE/RSJ International Conference on Intelligent Robots and Systems*, 1:399–406, 1995.

[19] J.K. Salisbury, B.S. Eberman, W.T. Townsend, and M.D. Levin. Design and control of an experimental whole-arm manipulator. *Proc. of the 1989 International Symposium on Robotics Research*, 1989.

[20] I. Sardellitti, J. Park, D. Shin, and O. Khatib. Air muscle controller design in the distributed macro-mini(dm^2) actuation approach. *Proc. of the 2007 IEEE/RSJ International Conf. on Intelligent Robots and Systems*, 2007.

[21] R. Schiavi, G. Grioli, S. Sen, and A. Bicchi. Vsa–ii: A novel prototype of variable stiffness actuator for safe and performing robots interacting with humans. *IEEE International Conference on Robotics and Automation*, 2008.

[22] D. Shin, I. Sardellitti, and O. Khatib. A hybrid actuation approach for human-friendly robot design. *Proc. of the 2008 IEEE International Conference on Robotics and Automation*, 2008.

[23] D. Shin, I. Sardellitti, Y. Park, O. Khatib, and M. Cutkosky. Design and control of a bio-inspired human-friendly robot. *to appear in Proc. of the 11th International Symposium on Experimental Robotics 2008*, 2008.

[24] P. Thaulad. Human friendly robot control system design and experimental validation. *Degree of Engineer Thesis, Stanford University, Stanford, CA*, 2005.

[25] B. Tondu and P. Lopez. Modeling and control of mckibben artificial muscle robot actuators. *IEEE Control Systems Magazine*, 30:15–38, 2000.

[26] B. Tondu and S.D. Zagal. Mickebben artificial muscle can be adapted to be in accordance with the hill skeletal muscle model. *IEEE Internation Conference on Biomedical Robotics and Biomechatronics*, 2006.

[27] G. Tonietti and A. Bicchi. Adaptive simultaneous position and stiffness control for a soft robot arm. *IEEE/RSJ International Conference on Intelligent Robots and Systems*, pages 1992–1997, 2002.

[28] G. Tonietti, R. Schiavi, and A. Bicchi. Design and control of a variable stiffness actuator for safe and fast physical human/robot interaction. *IEEE International Conference on Robotics and Automation*, pages 528–533, 2005.

[29] R. Van Ham, B. Vanderborght, M. Van Damme, B. Verrelst, and D. Lefeber. Maccepa, the mechanically adjustable compliance and controllable equilibrium position actuator: Design and implementation in a biped robot. *Robotics and Autonomous Systems*, 55(10):761–768, 2007.

[30] R. Van Ham, B. Verrelst, F. Daerden, and D. Lefeber. Pressure control with on-off valves of pleated pneumatic artificial muscles in a modular one-dimensional rotational joint. *International Conference on Humanoid Robots*, page 35, October 2003.

[31] B. Vanderborght, B. Verrelst, R. Van Ham, and D. Lefeber. Controlling a bipedal walking robot actuated by pleated pneumatic artificial muscles. *Robotica*, 24(4):401–410, 2006.

[32] L. E. Weiss, R. Merz, F. B. Prinz, G. Neplotnik, P. Padmanabhan, L. Schultz, and K. Ramaswami. Shape deposition manufacturing of heterogeneous structures. *Journal Of Manufacturing Systems*, 16(4):239–248, 1997.

[33] S. Wolf and G. Hirzinger. A new variable stiffness design: matching requirements of the next robot generation. *IEEE Inter. Conf. Robotics and Automation*, 2008.

[34] M. Zinn. A new actuation approach for human friendly robotic manipulation. *PhD thesis, Stanford University, Stanford, CA*, 2005.

[35] M. Zinn, O. Khatib, B. Roth, and J.K. Salisbury. New actuation approach for human-friendly robotics. *8th International Symposium on Experimental Robotics*, 2002.

[36] M. Zinn, B. Roth, O. Khatib, and J. K. Salisbury. New actuation approach for human-friendly robot design. *International Journal of Robotics Research*, 23(1):379–398, 2004.